Three-Dimensional Simulations of Multidetector Point-Focusing SPECT Imaging

Hee-Joung Kim, Barry R. Zeeberg, Murray H. Loew, and Richard C. Reba

Department of Radiology and Department of Electrical Engineering and Computer Science, George Washington University, Washington, DC

We have applied an efficient algorithm for mathematically simulating the three-dimensional (3-D) response of a SPECT imaging system with a depth-dependent 3-D point spread function (3-DPSF). The input object whose reconstructed image is to be simulated is restricted to a binary map; more complex objects may be treated as linear combinations of binary maps. The 3-D convolution reduces to a sequence of additions of a 3-D line spread function (3-DLSF), appropriately translated, to the 3-D response. We have simulated the projection data from a multidetector SPECT system with point-focusing collimators. The simulated projection data were then reconstructed using the manufacturer's software. The objects simulated included simple geometrical solids such as spheres and cylinders, as well as the distribution of muscarinic cholinergic receptors in a realistic brain slice. The results of these simulations indicate the existence of significant qualitative and quantitative artifacts in reconstructed human brain images.

J Nucl Med 1991; 32:333–338

U sing the mAChR-binding radioligand, (R,R)-$[^{123}I]$ 4IQNB, and a multidetector point-focusing single-photon emission computed tomography (SPECT) instrument, we have found apparent deficits in the posterior parietal cortex in normal volunteers and in Alzheimer's disease patients (*1,2*). These apparent deficits may be due to altered radioactivity localization or to imaging/ reconstruction artifacts. An identical point-focusing SPECT instrument has also been used to evaluate technetium-99m-ethyl cisteinate dimer (^{99m}Tc-ECD) as a cerebral blood flow agent in monkey and human (*3,4*).

The quantitative potential of SPECT or PET for estimating regional concentration of neuroreceptors or blood flow can be degraded by inaccuracies in kinetic modeling of radiotracer localization, as well as inaccuracies in image reconstruction. In particular, a shape-

and size-dependent recovery coefficient (RC) could cause two regions with identical radioactivity concentration artifactually to appear to have significantly different radioactivity concentrations in the reconstructed image. For example, this phenomenon would be troublesome in the case of the muscarinic cholinergic receptor, which is distributed uniformly throughout the grey matter of the cerebral cortex (*5*). In this case, there may be an apparent regional difference of radioligand localization caused by differing regional thicknesses of cortical grey matter.

Some of the basic papers that discuss the problems of partial volume effects and detector-aperture functions include Hoffman et al. (*6*), Mazziotta et al. (*7*), Kearfott et al. (*8*), and Mullani et al. (*9*). In spite of the importance of these degradations in the reconstruction process, there has been relatively little reported about three-dimensional (3-D) considerations in imaging physics (*10–15*); the central processing unit time required for performing the 3-D convolution for a 3-D imaging simulation may be prohibitive. If the object whose reconstructed image requiring simulation is restricted to being a binary map, an efficient algorithm for performing the 3-D convolution can be implemented. Even subject to this restriction, the simulation studies can provide useful information about the RCs of different brain regions.

We present here the results of applying an efficient algorithm for simulating the 3-D projection data resulting from a 3-D distribution of radioactivity. The algorithm was applied to a series of radioactive spherical and cylindrical mathematical phantoms of systematically varying size and to a realistic mathematical brain phantom. The results show that the RC for the geometric objects vary significantly and that different cortical regions can vary by a factor of 4.75. Thus, apparent differences in regional radioactivity concentration must be interpreted with care.

METHODS

The SPECT system used was the Strichman 810 (Fig. 1) with a 572-hole collimator and software version 2.51. We paraphrased the description of the physics of the multidetector
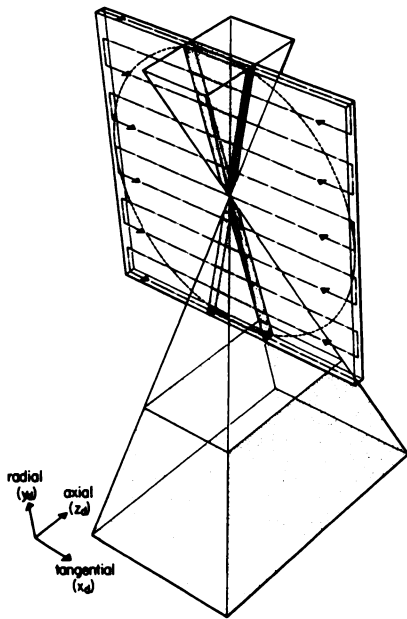
FIGURE 1
Illustration of outer "envelope" of collimator response function. The intersection of this "double-pyramid" envelope with a single slice of activity is shaded. Copied from Ref. 10.

point-focusing SPECT instrument given by Moore and Mueller (*10*): The instrument contains 12 scanning detectors, 30° apart around a circle. Each detector consists of one phototube viewing a large rectangular NaI(Tl) crystal. On the source side of the crystal is a point-focusing collimator. The collimator collects from the source those photons which emanate along a set of lines, all of which traverse the focal point. Thus, a measurement recorded by one detector at a single scan position represents an integral of counts over a solid angular bundle of projection rays. During the scanning of one transverse section, each detector assembly moves both tangentially and radially to the circular aperture such that its focal point "raster scans" through half the source circle. An opposing detector scans the other half of the circle. The *projection data* are acquired at each tangential and radial detector position, and stored as a two-dimensional array of 128 tangential by 12 radial positions. The detectors all perform raster scans simultaneously. Adjacent transverse sections are scanned by moving the patient couch axially out of the gantry and re-scanning. The intersection of the outer "envelope" of the collimator response function with the single slice of activity is illustrated in Figure 1. Most of the counts recorded when scanning an axially extended source emanate from transverse sections other than the central one. The projection data are *reconstructed* using an algorithm similar to that described by Stoddart and Stoddart (*16*).

The three-dimensional point-spread function (3-DPSF) was experimentally measured by acquiring the projection data for a cotton ball of 3 mm diameter containing ~300 uCi of ^{99m}Tc. Twenty slices of projection data at an axial interval of 3 mm were acquired starting at z = −100 mm, and 40 slices were acquired at an interval of 1 mm starting at z = −40 mm. These projection data were decay-corrected and then were used to represent a 3-DPSF with equal resolution (3 mm) in

the x, y, and z directions. *The 3-DPSF represented the projection data, not the reconstructed image,* and was normalized so that the integrated volume was equal to unity.

Mathematical models of objects to be simulated were constructed by packing 3 mm voxels within the 3-D object boundary. Geometric objects could be generated programatically; the extended brain slice was generated manually for a transverse slice through the basal ganglia, taken from a standard atlas (*17*). The slice was overlaid with a transparency containing a square grid with resolution 3 mm × 3 mm. Squares in the grid were either set to unity or to zero (Fig. 2), depending on whether more than one-half of the square overlapped the cerebral cortex or caudate nucleus, regions known to contain approximately the same concentrations of mAChR (*5*). The slice was extended axially to form a 3-D "brain slice cylinder" of 111 mm length. This model was chosen for our initial brain studies, since the manufacturer's reconstruction algorithm implicitly assumes that the object to be reconstructed has the same cross-section along its entire length. Thus, a brain slice cylinder more closely matches the assumptions of the reconstruction algorithm, and the reconstruction artifacts for a brain slice cylinder are expected to be less than those for a more realistic 3-D brain model.

There are three spatial convolution methods available for the simulation of the projection data resulting from imaging a radioactive object.

Method 1. For an object with arbitrary voxel values within an n x n x n voxel cubic field of view, convolution according to the standard definition would be computed as:

$$PROJ(i,j,k) = \Sigma_{i'}\Sigma_{j'}\Sigma_{k'} [OBJ(i',j',k')PSF(i-i'-, j-j'-, k-k')],$$

where PROJ is the simulated projection data, OBJ is the mathematical radioactive object, and PSF is the 3-DPSF represented as projection data. This computation is projection-driven. The projection data are represented as three-dimensional, since the physical process of multiple slice data acquisition for the point-focusing instrument involves tangential, radial, and axial components.

Method 2. If the nonzero voxels of the object only fill a portion of the field of view, then a more efficient procedure
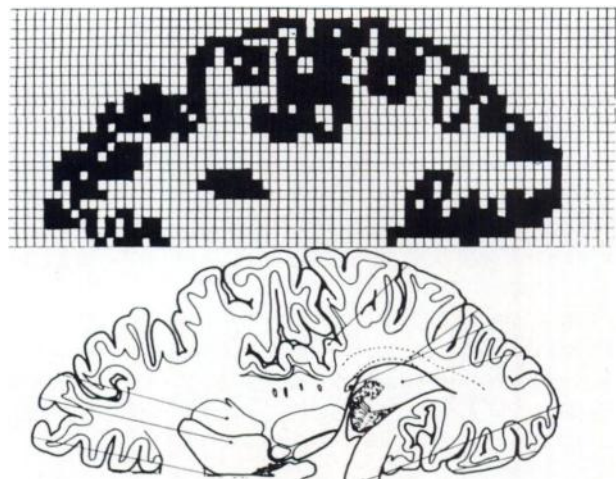

FIGURE 2
Standard brain atlas (*17*) transverse slice through the basal ganglia and manually digitized grey matter regions.

would be to build up the simulated projection data as the successive summation of projection data for each nonzero voxel: For each nonzero voxel, the 3-DPSF is multiplied by the voxel value, translated according to the voxel position, and summed into an array containing the accumulated simulated projection data. Symbolically, a nonzero voxel at position (i,j,k) contributes OBJ(i,j,k)PSF(i'-i,j'-j,k'-k) to PROJ(i',j',k'). This computation is object-driven.

Method 3. For an object with voxel values either equal to 0 or 1 (a binary map), a modification of Method 2 is possible in which 3-DLSFs (line-spread functions) instead of 3-DPSFs are translated and summed. Thus, the summation can be carried out just once for an axial run of w adjacent voxels of value 1, rather than w times as in Method 2. We used Method 3 for all of the simulations described here. Although the LSF could be computed for runs in the radial or tangential directions, we chose the axial direction since this guarantees the same algorithmic efficiency for the simulation of the projection data for each angular detector position. If the object is not cylindrically symmetrical, then the x- and y-coordinates in the object description are transformed by a rotation about the z-axis, so as to be consistent with the coordinate system defined by each detector. If the object is cylindrically symmetrical, then the projection data computed for one detector is simply copied to each of the remaining detectors. The requirement for a binary map is not a severe restriction, since (a) linear combinations of simulated projection data can be scaled and added, (b) for the purposes of computing RCs, voxel values of 1 are sufficient, and (c) for some systems, uniform radioactivity distributions may be a reasonably good approximation.

The interpretation of the numerical value of the RC depends on how the 3-DPSF is normalized. There are at least two possible plausible alternative normalizations. Normalize so that (a) the RC equals 1.0 in the reconstructed image of a large hot cylinder or (b) the volume under the physically measurable 3-DPSF equals unity. We chose the normalization described in (b), because the commercial reconstruction algorithm would perform an inappropriate background subtraction for a large cylinder. Because of the arbitrary nature of the selection of the normalization procedure, the absolute values of the RCs are arbitrary. Recovery coefficients computed using this normalization are approximately equal to 50% of those computed using normalization (a).

The recovery coefficient for the simulated projection data

was estimated from the maximum detector intensity value over all 12 detectors and over all (x,y,z) positions. The 3-DPSF will maximally overlap the object if the 3-DPSF is translated to this position as its center.

The simulated projection data were converted to the format required by the manufacturer's reconstruction software. The simulated projection data were reconstructed. A series of filters of different levels of resolution is provided by the manufacturer. These filters are proprietary and no information is available about their design. The highest resolution filter possible was used for all reconstructions, since no noise was present in any of the simulations. The reconstruction algorithm automatically performs a background subtraction based upon the radioactivity detected in certain positions of the projection data.

The reconstructed brain image of a normal subject was obtained 24 hr after i.v. injection of ~5 mCi of (R,R)-[^{123}I] IQNB, a specific radioligand for mAChR (*1,2*).

Circumferential cortical profiles were determined as described previously (*2,18*).

RESULTS

Validation Studies

The projection data for a hot cube (153 mm) simulated using the algorithm were identical to those computed by direct convolution (Method 1) with the 3-DPSF (data not shown).

The simulated reconstructed image (Fig. 3A) of a hot ring source (containing 3 mCi of ^{99m}Tc) centered at the origin (168 mm id, 171 mm od) and of 3 mm axial extent was symmetrical with respect to the origin, and displayed the "Hong Kong-dollar" effect (*19*). The physically measured reconstructed image of a similar ring source (144 mm id, 147 mm od) and of 3 mm axial extent also displayed the Hong Kong-dollar effect (not shown). The two Hong Kong-dollar effects were quantitatively compared using circumferential profiles, and found to be quantitatively similar (Fig. 3B). Deviations between the two circumferential profiles may be due to the different diameters of the two ring sources and to the variation of the 3-DPSF from detector to detector in the physically measured projection data.
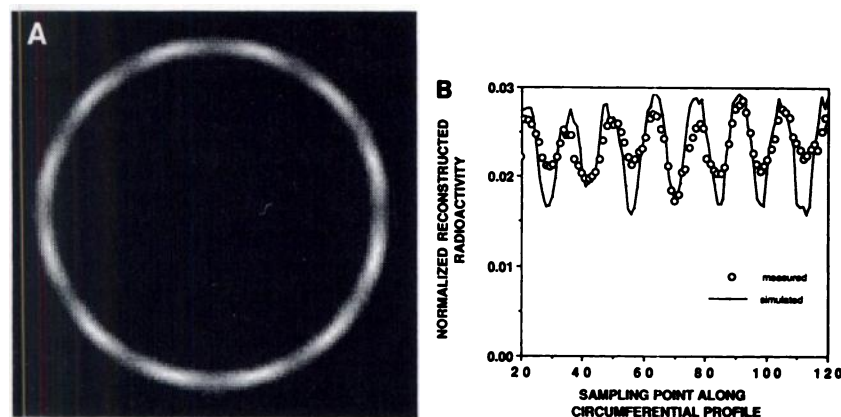

FIGURE 3
Hong Kong-dollar effect in the simulated reconstructed image of a 3-mm thick ring (A). Circumferential profiles for the simulated and physically measured reconstructed image of a 3-mm thick ring (B).

Recovery Coefficient

The central voxel value for the reconstructed image of a large hot cylinder centered at the origin (201 mm diameter; 153 mm axial extent) was 0.48 (Fig. 4). This value is numerically equal to the RC, since the theoretical value is unity. This value is based upon the arbitrarily chosen normalization of the 3-DPSF so that the volume under the physically measurable 3-DPSF equals unity. The value for the RC would be elevated if an automatic background subtraction had not been performed.

The projection data for a series of 14 spheres centered at the origin were simulated and reconstructed. The RCs based upon the projection data increase in a nearly linear manner with increasing diameter, whereas the RCs based upon the reconstructed images have a very strong dependence upon diameter up to 20 mm and then plateau at RC =0.40 (Fig. 4).

Projection data and reconstructed images of a series of 15 cylinders centered at the origin were simulated. The RCs based upon the projection data increase in a nearly linear manner with increasing diameter, whereas the RCs based upon the reconstructed images have a very strong dependence upon diameter up to 20 mm and then plateau slightly below the plateau for the spheres (Fig. 4).

The RCs (Fig. 4) based upon the projection data for two series of spheres located at (0,0,0) or (0,72,0) were identical for both positions; the RC based upon the reconstructed images deviated for diameters greater than 33 mm.

Extended Brain Slice

The image of a physically measured normal human brain was reconstructed using the automatically-selected (relatively low-resolution) filter (Fig. 5A). The simulated extended brain slice image using the same filter demonstrates qualitative degradations (Fig. 5B). There are qualitative similarities between the two re-
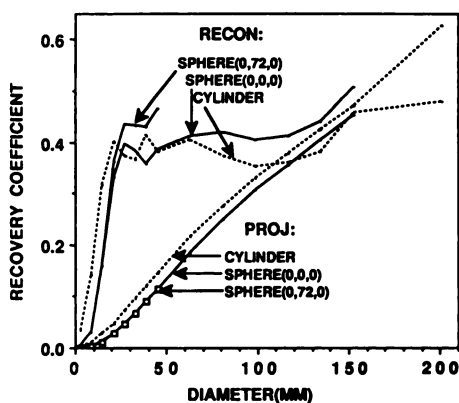

FIGURE 5
Reconstructed image of a physically imaged normal human brain (A) and a simulated brain slice cylinder (B).

constructed images, although the slices are at somewhat different anatomic levels, and the simulated brain is more opened since it was not confined to the inside of a skull. Circumferential profiles (2,18) provide a quantitative estimate of the apparent cortical deficits, particularly in the posterior parietal region (Fig. 6). The circumferential profile for the simulated reconstructed image using a high-resolution filter (Fig. 6) shows that an apparent 4.75-fold variation in regional radioactivity concentration can artifactually arise from regions that are of identical radioactivity concentration.

DISCUSSION

We present here the results of applying an efficient algorithm for simulating the 3-D projection data resulting from a 3-D distribution of radioactivity. The algorithm was applied to a series of radioactive spherical and cylindrical mathematical phantoms of systematically varying size, and to a realistic mathematical brain phantom.

The quantitative accuracy of our simulation proce-

FIGURE 4
Recovery coefficients for the projection and reconstructed images of series of spheres centered at (0,0,0) and (0,72,0) and cylinders centered at (0,0,0).
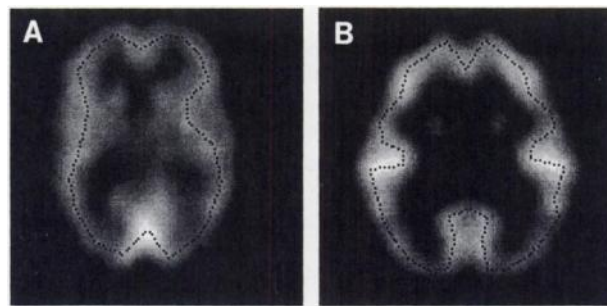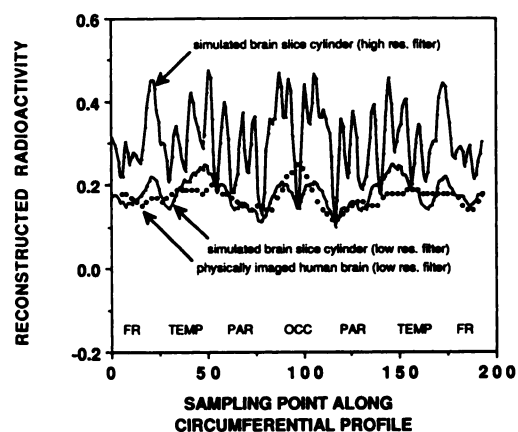

FIGURE 6
Circumferential profiles for the cortical regions of the reconstructed images of a physically imaged normal human brain and a simulated brain slice cylinder. The circumferential profile for the physically imaged normal human brain was scaled so that its maximum was equal to the maximum for the simulated brain slice cylinder using the low-resolution filter.

dure was demonstrated by reproducing the pattern of artifacts known as the Hong Kong-dollar effect (Fig. 3). Thus, the simulation procedure is able to mimic subtleties of the physical imaging and reconstruction process.

One of the simplest objects studied was a large cylinder. It is expected that the RC for the reconstructed image of such a large object would be close to unity. However, the RC is significantly less than unity (Fig. 4). This lack of absolute quantification results, in part, from the automatically-performed background subtraction, from an inexact reconstruction algorithm, and possibly from the fact that the scanning pattern covers a finite rather than an infinite spatial extent (10).

The sharp dependence of the RC in the reconstructed image upon the size of spheres of less than 20 mm diam (Fig. 4) can significantly degrade quantitative accuracy in neuroimaging, since the sizes of many anatomical brain structures are within this range (Table 1). Thus, the apparent regional radioactivity in an approximately spherical region is strongly dependent on size in addition to the actual radioactivity concentration. The size dependence of the RC in the reconstructed image is sharper than that in the projection data (Fig. 4), so that the reconstruction algorithm apparently increases the dependence upon size.

The reconstructed image of the simulated extended brain slice (Figs. 5B) demonstrates the qualitative and quantitative degradations that might be expected in the reconstructed images of a real brain. Although the simulation omitted many factors which degrade a real reconstruction (attenuation, noise, scatter, nonuniform object cross-section), there are qualitative similarities with a reconstructed brain image (Figs. 5A) of a normal subject. The circumferential profiles derived from the simulated brain provide a quantitative estimate of the contribution of imaging artifact to the apparent cortical deficits (Fig. 6), particularly in the posterior parietal region. Not only is the RC significantly less than unity, but the circumferential profile for the simulated image reconstructed using the high-resolution filter (Fig. 6) shows that an apparent 4.75-fold variation in regional radioactivity concentration can artifactually arise from regions that are theoretically of identical radioactivity concentration. There are significant deficits in the reconstructed image of the simulated data, even though the mathematical model had no deficit. The same types

of artifacts that we have demonstrated in the simulated images may also occur in the physically measured images of human subjects (Fig. 6).

The high frequency variation in the high-resolution circumferential profile for the simulated extended brain slice (Fig. 6) is not the result of noise or statistical fluctuation, since the simulations were noise-free. These variations are completely deterministic and are a function of the angular position of the detectors relative to the brain slice, the 3-D spatial dependence of the cortical thickness, and the position and orientation of the cortical regions. To further distinguish the deterministic variation in Figure 6 from a variation due to random statistical noise, we note that a periodic variation was generated as the result of detector position for a uniform hot ring (Fig. 3). These types of artifacts contribute to the high frequency variation in the circumferential profile of the noise-free simulated reconstructed image (Fig. 6).

Preliminary simulation studies with a parallel-hole SPECT system exhibit qualitatively and quantitatively similar variations (not shown). The exact quantitative comparison remains to be completed. Thus, the artifacts seen with the point-focusing system are generalized to the more common parallel-hole systems.

CONCLUSIONS

The size dependence of the RC arises in the imaging process, as demonstrated here in the RCs for the projection data. The manufacturer's reconstruction algorithm further intensifies the size dependence. The dependence of reconstructed radioactivity concentration upon shape, size, and orientation is directly translated into qualitative and quantitative artifacts in the reconstructed image of a simulated or physically imaged brain. For example, simulations with a realistic extended brain slice indicate a 4.75-fold variation in the reconstructed radioactivity concentrations in cortical regions that are of equal radioactivity concentration. This result casts considerable doubt upon the ability of the current multidetector point-focusing SPECT system to quantitate regional radioactivity concentration accurately. Possible solutions currently under evaluation in simulation studies include: increasing the number of detectors, increasing resolution, improving the reconstruction algorithm, or using triple-headed rotating parrallel-hole rather than multidetector point-focusing SPECT. Thus, the simulation algorithm described here will be used to evaluate the effects of altered instrument design and reconstruction algorithms in improving the quantitative accuracy of SPECT neuroimaging.

TABLE 1
Neuroanatomical Structure Volumes

Structure	Volume (cc)	Diameter (mm)	Reference
Caudate	5.2	10.7	7
Putaman	5.1	10.7	7
Thalamus	5.0	10.6	7
Cerebellum	141.0	32.3	20

REFERENCES

1. Holman BL, Gibson RE, Hill TC, Eckelman WC. Muscarinic acetylcholine receptors in Alzheimer's disease in vivo imaging with iodine-123-labeled 3-quinuclidinyl-4-iodobenzilate and emission tomography. *JAMA* 1985;254:3063–3066.

2. Kim HJ, Zeeberg BR, Gibson RE, Hosain P, Wesley R, Reba RC. SPECT study of the localization of R,R-[^{123}I]IQNB in Alzheimer's patients and normals [Abstract]. *J Nucl Med* 1990;31:729.

3. Walovitch RC, Hill TC, Garrity ST, et al. Characterization of technetium-99m-L,L-ECD for brain perfusion imaging, part 1: pharmacology of technetium-99m-ECD in nonhuman primates. *J Nucl Med* 1989;30:1892–1901.

4. Leveille J, Demonceau G, De Roo M, et al. Characterization of technetium-99m-L,L-ECD for brain perfusion imaging. 2. Biodistribution and brain imaging in humans. *J Nucl Med* 1989;30:1902–1910.

5. Davies P, Verth AH. Regional distribution of muscarinic acetylcholine receptor in normal and Alzheimer's-type dementia brains. *Brain Res* 1978;138:385–392.

6. Hoffman HJ, Huang S-C, Phelps ME. Quantitation in positron emission computed tomography. 1. Effect of object size. *J Comp Assist Tomog* 1979;3:299–308.

7. Mazziotta JC, Phelps ME, Plummer D, Kuhl DE. Quantitation in positron emission computed tomography. 5. Physical-anatomical effects. *J Comp Assist Tomog* 1981;5:734–743.

8. Kearfott KJ, Kluksdahl EM. Effects of axial spatial resolution and sampling on object detectability and contrast for multiplanar positron emission tomography. *Med Phys* 1989;16:785–790.

9. Mullani NA. A phantom for quantitation of partial volume effects in SPECT. *IEEE Trans Nucl Sci* 1989;36:983–987.

10. Moore SC, Mueller SP. Inversion of the 3D Radon transform for a multidetector, point-focused SPECT brain scanner. *Phys Med Biol* 1986;31:207–221.

11. Rusinek H, Youdin M, Reich T. Reconstruction of isotope distribution in the brain: error analysis for instrument design. *Ann Biomed Eng* 1978;6:399–412.

12. Hsieh RC, Wee WG. On methods of three-dimensional reconstruction from a set of radioisotope scintigrams. *IEEE Trans Sys Man Cyb* 1976;SMC-6:854–862.

13. Ying-Lie O. An ECAT reconstruction method which corrects for attenuation and detector response. *IEEE Trans Nucl Sci* 1983;NS-30:632–636.

14. Formiconi AR, Pupi A, Passeri A. Compensation of spatial system response in SPECT with conjugate gradient reconstruction technique. *Phys Med Biol* 1989;34:69–84.

15. Zeeberg BR, Bice AN, Loncaric S, Wagner HN Jr. A theoretically-correct algorithm to compensate for a three-dimensional spatially-variant point spread function in SPECT imaging. In: Graaf CN, Viergever MA, eds. *Proceedings of the 10th international conference of information processing in medical imaging.* New York: Plenum Press; 1988:245–254.

16. Stoddart HF, Stoddart HA. A new development in single gamma transaxial tomography Union Carbide focused collimator scanner. *IEEE Trans Nucl Sci* 1979;26:2710–2712.

17. DeArmond S, Fusco MM, Dewey M. *A photographic atlas structure of the human brain,* 2nd edition. New York: Oxford University Press; 1976:17–36.

18. Links JM, Loats HL, Holcomb HH, Loats SE, Stumpf MJ, Wagner HN Jr. Cortical circumferential profiling: an objective approach to cortical quantification in emission tomography [Abstract]. *J Nucl Med* 1989;30:816.

19. Moore SC, Doherty MD, Zimmerman RE, Khul DE. Improved performance from modifications to the multidetector SPECT brain scanner. *J Nucl Med* 1984;25:688–691.

20. Kennedy DN, Filipek PA, Caviness VS Jr. Anatomic segmentation and volumetric calculations in nuclear magnetic resonance imaging. *IEEE Trans Med Imag* 1989;8:1–7.